ZVS Boundary Analysis and Optimization Strategy of Phase-Shift Values for Three-Level Dual-Active-Bridge Converters Using Harmonic Decomposition

Wei Shao, Chenchen Wang, *Senior Member, IEEE*, Kai Li, *Member, IEEE*, Zhibo Zhang, *Graduate Student Member, IEEE*, and Changyu Gao, *Graduate Student Member, IEEE*

***Abstract*—The dual-active-bridge (DAB) converter, comprising a primary-side three-level neutral-point-clamped bridge and a secondary-side H-bridge, represents a promising topology for voltage conversion applications between medium-voltage dc and low-voltage dc. To ensure efficient operation under high-frequency conditions, it is imperative to realize a wide zero-voltage-switching (ZVS) range. In this article, the harmonic decomposition method is utilized to analyze the ZVS boundaries and derive a universal piecewise model without complex multimodal analysis. A simple and practical ZVS optimization strategy of phase-shift values is proposed for three-level DAB converters to realize ZVS across the maximum possible θ range. It is extended further to M-level-to-N-level DAB converters to become a universal method for ZVS implementation. The derived ZVS boundaries and the proposed parameter design methods are verified through simulation and experimental results.**

***Index Terms*—Harmonic decomposition method, multilevel dual-active-bridge (DAB) converter, quadra-phase-shift (QPS) modulation, zero voltage switching (ZVS).**

I. Introduction

THE dual active bridge (DAB) converter, with its inherent bidirectional power flow capability and advantages of high efficiency, galvanic isolation, as well as high power density, is the most commonly used topology for dc–dc applications [1], [2]. Compared with traditional DAB converters, multilevel DAB converters are more suitable for higher power applications since they possess higher voltage blocking capability, a higher step-up ratio, and more control degrees of freedom, enhancing the performance of converters. For applications with considerably different input and output rated voltages, it is more practical to adopt three-level DAB converters to avoid the use of switching devices operating at excessively high voltages. For instance, Fig. 1 depicts an ac–dc solid-state transformer (SST) [3] with submodules featuring 1.5 kV dc ports and 700 V dc ports. While the half-bridge neutral-point-clamped (NPC) topology and series half bridge [4] can be alternative for the high-voltage-side topology, they are not suitable for high current applications. Furthermore, the active neutral-point-clamped structure [5] increases costs and control complexity because of the two additional switching devices per bridge arm. Consequently, a three-level DAB converter with a full-bridge NPC topology on the high-voltage side and an H-bridge on the low-voltage side emerges as a promising alternative [6], as depicted in Fig. 2.

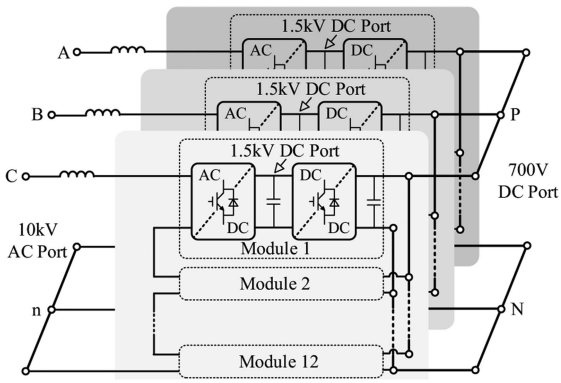

Fig. 1. Structure of an AC–DC-SST.

In the field of DAB converters, the adoption of wide-bandgap power devices, such as Gallium-Nitride and Silicon Carbide, opens up avenues for improving operational frequency and power density [7]. However, raising switching frequency without implementing zero-voltage-switching (ZVS) leads to higher switching losses, lower power density, thermal dissipation challenges, high-frequency switching noise, and electromagnetic interference [8]. Therefore, achievement of the widest possible range of ZVS is crucial for efficient high-frequency performance of DAB.

Various studies have been conducted to identify ZVS range for DAB converters, most often using piecewise linear methods

Received 10 December 2024; revised 20 March 2025; accepted 20 April 2025. Date of publication 25 April 2025; date of current version 30 June 2025. This work was supported by the National Key Research and Development Program of China under Grant 2023YFB4004600. Recommended for publication by Associate Editor J. Lam. *(Corresponding author: Kai Li.)*

The authors are with the School of Electrical Engineering, Beijing Jiaotong University, Beijing 100044, China (e-mail: 22121498@bjtu.edu.cn; chchwang@bjtu.edu.cn; kaili@bjtu.edu.cn; zbzhang@bjtu.edu.cn; changyugao@bjtu.edu.cn).

Color versions of one or more figures in this article are available at https://doi.org/10.1109/TPEL.2025.3564517.

Digital Object Identifier 10.1109/TPEL.2025.3564517

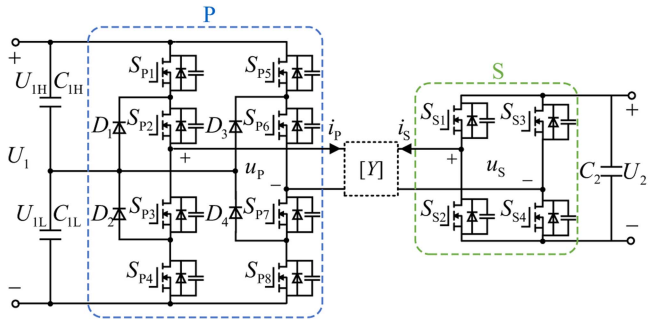

Fig. 2. Topology of the three-level DAB converter.

in the time domain. In [9], ZVS conditions are given for four operating modes under triple-phase-shift (TPS) modulation, and a multiobjective optimization was achieved by applying particle swarm optimization algorithm. In [10], the ZVS range for three-level DAB converters is determined under dual-phase-shift (DPS) modulation through multimodal analysis. However, the piecewise linear method assumes an ideal coupling network between the two bridges, which hinders simple incorporation of complex ac coupling network and various practical issues such as dead time and device parasitic capacitances. In addition, this method offers numerical solutions for ZVS implementation, and become much more complicated with more degrees of freedom. In contrast, analyses based on harmonic decomposition can determine ZVS ranges without multiple operating mode analysis [11], [12]. In [13], ZVS boundaries considering complex ac coupling units and non-ideal factors are obtained for traditional DAB converters, together with an analytical solution to implement the widest possible ZVS range. Khanzadeh and Thiringer [14] presented closed-form equations and simplified approximations for the ZVS boundaries of three-phase *M*-level-to-*N*-level (*M*L/*N*L) DAB converters, enabling the exploration of various factors such as winding configurations and dead time. However, limited studies offer simple analytical solutions for practical ZVS realization of the topology presented in Fig. 2.

This article analytically determines the ZVS boundaries of three-level DAB converters across the entire operating range through a harmonic decomposition-based analysis. A simple ZVS optimization strategy for phase-shift values is proposed to achieve a wide ZVS range for *M*L/*N*L DAB converters. The rest of this article is organized as follows. In Section II, the ZVS boundary of the three-level DAB converter is derived based on the quadra-phase-shift modulation (QPS). In Section III, the ZVS range is illustrated and the ZVS optimization strategy is derived. Moreover, the proposed strategy is expanded to the *M*L/*N*L DAB converter. In Section IV, nonideal factors like dead time and switching devices' capacitance are considered to present practical ZVS range. In Section V, the experimental and simulation results are given to verify the derived ZVS range and the proposed ZVS optimization strategy. Finally, Section VI concludes this article.

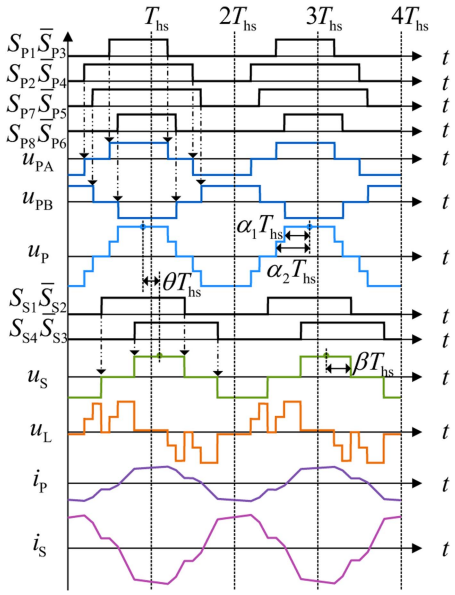

Fig. 3. General waveforms of QPS modulation.

II. Operating Principle and ZVS Boundary of Three-Level DAB Converters

A. Operating Principle Under Quadra-Phase-Shift Modulation

The typical topology of a three-level DAB converter is illustrated in Fig. 2, employing a full-bridge NPC converter on the primary side and a H-bridge on the secondary side. The primary- and secondary-side converters are connected via a high-frequency transformer (HFT) denoted by a two-port coupling unit, whose admittance is denoted by [*Y*]. S_{Px} ($x = 12, \ldots, 8$) and S_{Sy} ($y = 12, \ldots, 4$) represent switching devices on the primary and secondary sides, respectively. i_P and i_S denote primary- and secondary-side currents. U_1 and U_2 represent the input and output dc voltages. u_P and u_S signify the ac-side voltages of the transformer with a turns-ratio of n:1. The voltage conversion ratio is defined as $d = nU_2/U_1$.

The four degrees of freedom are fully exploited to realize QPS modulation, as depicted in Fig. 3. θ represents the outer phase-shift value governing power flow direction, α_1, α_2, and β are duty-cycle ratios modulating voltage magnitudes. Other phase-shift modulation methods can be taken as special cases of the unified form. The single-phase shift modulation is achieved when $\alpha_1 = \alpha_2 = \beta = 0.5$, the extended-phase shift modulation is achieved when $\alpha_1 = \alpha_2 = 0.5$ or $\beta = 0.5$, the DPS modulation is achieved when $\alpha_1 = \alpha_2 = \beta$, the TPS modulation is achieved when $\alpha_1 = \alpha_2$. To prevent voltage waveforms from concavity and ensure the switching signals within a single carrier cycle, the operating constraints can be summarized as

$$\begin{cases} 0 \le \alpha_1 \le \alpha_2 \le 0.5 \\ 0 \le \beta \le 0.5 \\ |\theta| \le \min\{2\alpha_1, 2\beta\}. \end{cases} \tag{1}$$

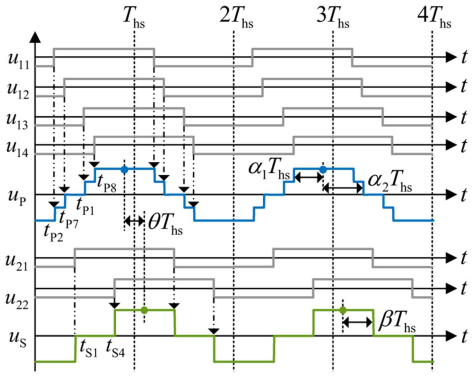

Fig. 4. Schematic diagram of AC-side voltage decomposition.

B. ZVS Boundary Derivation Using Harmonic Analysis

The relationship between the ac-side voltages and currents of the ac coupling network can be denoted by a two-port system as

$$\begin{bmatrix} i_{\mathrm{P}}(t) \\ i_{\mathrm{S}}(t) \end{bmatrix} = \begin{bmatrix} y_{\mathrm{P,P}}(t) & y_{\mathrm{P,S}}(t) \\ y_{\mathrm{S,P}}(t) & y_{\mathrm{S,S}}(t) \end{bmatrix} \begin{bmatrix} u_{\mathrm{P}}(t) \\ u_{\mathrm{S}}(t) \end{bmatrix} \tag{2}$$

where $y_{\mathrm{P,P}}(t)$ and $y_{\mathrm{S,S}}(t)$ denote self-admittances, $y_{\mathrm{P,S}}(t)$ and $y_{\mathrm{S,P}}(t)$ represent mutual admittances. The turns ratio n is considered in matrix $[Y]$. The ac-side voltages u_{P} and u_{S} can be formed by the superposition of square waves of 50% duty ratio corresponding to the switching instants, as shown in (3). The voltages together with their decomposed square waves are illustrated in Fig. 4

$$\begin{cases} u_{\mathrm{P}} = u_{11} + u_{12} + u_{13} + u_{14} \\ u_{\mathrm{S}} = u_{21} + u_{22} \end{cases}. \tag{3}$$

Given that a square wave can be represented as a summation of odd harmonics through a Fourier series expansion, the ac-side voltages and currents in (2) can be expressed in their Fourier series form similarly. For each of the harmonic frequencies, the time varying relationships between the voltages and currents can be expressed using the phasor theory [13] as

$$\begin{bmatrix} I_{\mathrm{P}}^k \angle \theta_{\mathrm{P}}^k \\ I_{\mathrm{S}}^k \angle \theta_{\mathrm{S}}^k \end{bmatrix} = \frac{1}{k\pi} \begin{bmatrix} Y_{\mathrm{P,P}}^k \angle \gamma_{\mathrm{P,P}}^k & Y_{\mathrm{P,S}}^k \angle \gamma_{\mathrm{P,S}}^k \\ Y_{\mathrm{S,P}}^k \angle \gamma_{\mathrm{S,P}}^k & Y_{\mathrm{S,S}}^k \angle \gamma_{\mathrm{S,S}}^k \end{bmatrix} \times \begin{bmatrix} U_{\mathrm{P}}^k \angle \varphi_{\mathrm{P}}^k \\ U_{\mathrm{S}}^k \angle \varphi_{\mathrm{S}}^k \end{bmatrix} \tag{4}$$

where

$$U_{\mathrm{P}}^k \angle \varphi_{\mathrm{P}}^k = U_1 \sum_{i=1.2} \angle k\pi \left(\frac{\theta}{2} - \alpha_i \right) - U_1 \sum_{i=1.2} \angle k\pi \left(\frac{\theta}{2} + \alpha_i \right)$$

$$U_{\mathrm{S}}^k \angle \varphi_{\mathrm{S}}^k = 2U_2 \angle k\pi \left(-\frac{\theta}{2} - \beta \right) - 2U_2 \angle k\pi \left(-\frac{\theta}{2} + \beta \right)$$

and k denotes the harmonic number. $Y_{\mathrm{P,P}}^k$, $Y_{\mathrm{P,S}}^k$, $Y_{\mathrm{S,P}}^k$, and $Y_{\mathrm{S,S}}^k$ represent the magnitude of the admittance phasors, and $\gamma_{\mathrm{P,P}}^k$, $\gamma_{\mathrm{P,S}}^k$, $\gamma_{\mathrm{S,P}}^k$, and $\gamma_{\mathrm{S,S}}^k$ are the phase angles of the admittance phasors. By converting (4) back into a sinusoidal steady-state time-varying form for each harmonic frequency and summing

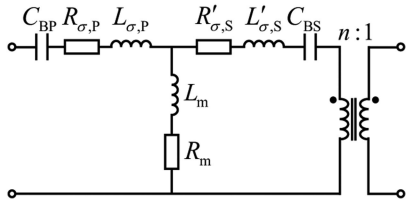

Fig. 5. Complex AC coupling network.

up all harmonic components, the ac-side currents are given as

$$i_{\mathrm{P}}(\omega t) = -\tfrac{2}{\pi} \textstyle\sum_{k=1,3,5\cdots}^{+\infty} \tfrac{1}{k} \times \begin{Bmatrix} U_1 Y_{\mathrm{P,P}}^k \left[\sin(k\alpha_1\pi) + \sin(k\alpha_2\pi)\right] \cos\left[k\left(\omega t + \frac{\theta}{2}\pi\right) + \gamma_{\mathrm{P,P}}^k\right] \\ +2U_2 Y_{\mathrm{P,S}}^k \sin(k\beta\pi) \cos\left[k\left(\omega t - \frac{\theta}{2}\pi\right) + \gamma_{\mathrm{P,S}}^k\right] \end{Bmatrix} \tag{5}$$

$$i_{\mathrm{S}}(\omega t) = -\tfrac{2}{\pi} \textstyle\sum_{k=1,3,5\cdots}^{+\infty} \tfrac{1}{k} \times \begin{Bmatrix} U_1 Y_{\mathrm{S,P}}^k \left[\sin(k\alpha_1\pi) + \sin(k\alpha_2\pi)\right] \cos\left[k\left(\omega t + \frac{\theta}{2}\pi\right) + \gamma_{\mathrm{S,P}}^k\right] \\ +2U_2 Y_{\mathrm{S,S}}^k \sin(k\beta\pi) \cos\left[k\left(\omega t - \frac{\theta}{2}\pi\right) + \gamma_{\mathrm{S,S}}^k\right] \end{Bmatrix} \tag{6}$$

where ω indicates the switching frequency. ZVS turn-ON can be realized when the voltage across the switching device becomes zero before turning it on. This can be achieved by conducting the parallel connected diode before turning the device on with the help of a negative current. The specific ZVS conditions considering half-cycle odd-symmetry can be given by

$$\begin{cases} i_{\mathrm{P}}(t_{\mathrm{P2}}) \le 0, i_{\mathrm{P}}(t_{\mathrm{P7}}) \le 0, i_{\mathrm{P}}(t_{\mathrm{P1}}) \le 0, i_{\mathrm{P}}(t_{\mathrm{P8}}) \le 0 \\ i_{\mathrm{S}}(t_{\mathrm{S1}}) \le 0, i_{\mathrm{S}}(t_{\mathrm{S4}}) \le 0 \end{cases} \tag{7}$$

where $t_{\mathrm{P2}} = (-\theta/2+\alpha_1)T_{\mathrm{hs}}$, $t_{\mathrm{P7}} = (-\theta/2+\alpha_2)T_{\mathrm{hs}}$, $t_{\mathrm{P1}} = (1-\theta/2-\alpha_2)T_{\mathrm{hs}}$, $t_{\mathrm{P8}} = (1-\theta/2-\alpha_1)T_{\mathrm{hs}}$, $t_{\mathrm{S1}} = (\theta/2+\beta)T_{\mathrm{hs}}$, and $t_{\mathrm{S4}} = (1+\theta/2-\beta)T_{\mathrm{hs}}$ are the turn-ON moments of corresponding switching devices. After substituting these instants into (7), the ZVS boundaries can be derived. If the coupling network is regarded as an inductor and an ideal transformer, the ac coupling network can be given by

$$\begin{cases} Y_{\mathrm{P,P}}^k \angle \gamma_{\mathrm{P,P}}^k = \frac{1}{k\omega L_{\mathrm{s}}} \angle -\frac{\pi}{2}, Y_{\mathrm{S,S}}^k \angle \gamma_{\mathrm{S,S}}^k = \frac{n^2}{k\omega L_{\mathrm{s}}} \angle -\frac{\pi}{2} \\ Y_{\mathrm{P,S}}^k \angle \gamma_{\mathrm{P,S}}^k = Y_{\mathrm{S,P}}^k \angle \gamma_{\mathrm{S,P}}^k = \frac{n}{k\omega L_{\mathrm{s}}} \angle \frac{\pi}{2}. \end{cases} \tag{8}$$

Then, the simplified ZVS boundaries are obtained as (9)–(14) shown at the bottom of the next page. Considering the complex equivalent circuit of HFT in Fig. 5, the coupling network can be expressed as (A1) in Appendix A, and the corresponding ZVS boundaries can be derived similarly.

III. ZVS Range Analysis and ZVS Optimization for Phase-Shift Values

A. Universal Piecewise ZVS Boundaries

Given specific α_1, α_2, and β, ZVS range shown in Fig. 6 can be obtained based on (9)–(14). Each colored line represents the ZVS boundary of the switching device. For example, S_{P8} (S_{P6}) can maintain ZVS below the purple line and achieve critical

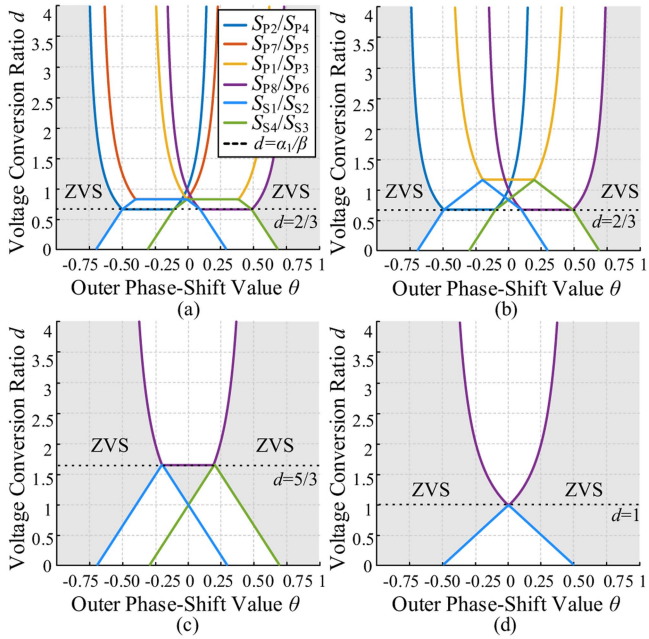

Fig. 6. Ideal ZVS range of the three-level DAB converter. (a) $\alpha_1 = 0.2$, $\alpha_2 = 0.3$, $\beta = 0.3$. (b) $\alpha_1 = 0.2$, $\alpha_2 = 0.5$, $\beta = 0.3$. (c) $\alpha_1 = 0.5$, $\alpha_2 = 0.5$, $\beta = 0.3$. (d) $\alpha_1 = 0.5$, $\alpha_2 = 0.5$, $\beta = 0.5$.

ZVS ON it. All primary-side switching devices can achieve ZVS below the union of the dark blue, orange, yellow, and purple lines, while secondary-side ones can implement ZVS above the blue and green lines. The full ZVS range is indicated by the gray area.

As shown in Fig. 6(a), when phase-shift values deviate from 0.5, QPS is achieved and there are six distinct ZVS boundaries. As α_2 increases [see Fig. 6(a) and (b)], the orange and yellow lines corresponding to (10) and (11) will shift to the upper right and the upper left, while the secondary-side boundaries shift upward. When α_2 equals 0.5, S_{P7} and S_{P1} activate simultaneously, producing two overlapping boundaries (the orange and yellow lines), as depicted in Fig. 6(b). It is worth noting that the intersection points of the outermost ZVS boundaries remain unchanged. As α_1 increases [see Fig. 6(b) and (c)], the dark blue and purple lines corresponding to (9) and (12) will shift to the upper right and the upper left, respectively, while other boundaries move only along the vertical axis. In the case where both α_1 and α_2 are set to 0.5, S_{P2}, S_{P7}, S_{P1}, and S_{P8} switch concurrently, leading to the coincidence of four upper boundaries under EPS, as shown in Fig. 6(c). As β increases [see Fig. 6(c) and (d)], the blue and green lines corresponding to (13) and (14) will shift to the lower right and the lower left, respectively, while other boundaries move only along the vertical axis. When α_1, α_2, and β are all set to 0.5, S_{S1} and S_{S4} switch simultaneously, aligning the two lower ZVS boundaries under SPS, as depicted in Fig. 6(d).

It can be seen that the primary-side ZVS boundaries are composed of no more than two curves with inverse proportional functions and a linear segment, and the secondary-side ZVS boundaries are comprised of a maximum of five linear segments. This naturally leads to the exploration of converting the boundaries in the Fourier series form into a piecewise model. Through mathematical derivation, the universal piecewise model is presented in Table I. Note that the cornerstone is (B3), whose detailed derivation is summarized in Appendix B.

B. ZVS Optimization for Phase-Shift Values

To achieve ZVS operation of the switching devices, each operating point must lie in the gray area by selecting appropriate phase-shift values. However, many points are available at a given transmission power, making the selection process challenging in practice. Also, it can be seen that the three-level DAB converter cannot realize ZVS in some cases. Thus, the crux of the matter is to find a simple and practical method to achieve ZVS across

$$2d\sum_{k=1,3,5\cdots}^{+\infty}\frac{1}{k^2}\sin(k\beta\pi)\sin\left[k\left(\alpha_1-\theta\right)\pi\right]-\sum_{k=1,3,5\cdots}^{+\infty}\frac{1}{k^2}\left[\sin(k\alpha_1\pi)+\sin(k\alpha_2\pi)\right]\sin\left(k\alpha_1\pi\right)\le 0 \tag{9}$$

$$2d\sum_{k=1,3,5\cdots}^{+\infty}\frac{1}{k^2}\sin(k\beta\pi)\sin\left[k\left(\alpha_2-\theta\right)\pi\right]-\sum_{k=1,3,5\cdots}^{+\infty}\frac{1}{k^2}\left[\sin(k\alpha_1\pi)+\sin(k\alpha_2\pi)\right]\sin\left(k\alpha_2\pi\right)\le 0 \tag{10}$$

$$2d\sum_{k=1,3,5\cdots}^{+\infty}\frac{1}{k^2}\sin(k\beta\pi)\sin\left[k\left(\alpha_2+\theta\right)\pi\right]-\sum_{k=1,3,5\cdots}^{+\infty}\frac{1}{k^2}\left[\sin(k\alpha_1\pi)+\sin(k\alpha_2\pi)\right]\sin\left(k\alpha_2\pi\right)\le 0 \tag{11}$$

$$2d\sum_{k=1,3,5\cdots}^{+\infty}\frac{1}{k^2}\sin(k\beta\pi)\sin\left[k\left(\alpha_1+\theta\right)\pi\right]-\sum_{k=1,3,5\cdots}^{+\infty}\frac{1}{k^2}\left[\sin(k\alpha_1\pi)+\sin(k\alpha_2\pi)\right]\sin\left(k\alpha_1\pi\right)\le 0 \tag{12}$$

$$\sum_{k=1,3,5\cdots}^{+\infty}\frac{1}{k^2}\left[\sin(k\alpha_1\pi)+\sin(k\alpha_2\pi)\right]\sin\left[k\left(\theta+\beta\right)\pi\right]-2d\sum_{k=1,3,5\cdots}^{+\infty}\frac{1}{k^2}\sin(k\beta\pi)\sin\left(k\beta\pi\right)\le 0 \tag{13}$$

$$\sum_{k=1,3,5\cdots}^{\infty}\frac{1}{k^2}\left[\sin(k\alpha_1\pi)+\sin(k\alpha_2\pi)\right]\sin\left[k\left(\beta-\theta\right)\pi\right]-2d\sum_{k=1,3,5\cdots}^{\infty}\frac{1}{k^2}\sin(k\beta\pi)\sin\left(k\beta\pi\right)\le 0 \tag{14}$$

TABLE I
UNIVERSAL PIECEWISE MODEL OF ZVS BOUNDARIES

Switching devices	ZVS ranges	θ range
S_{P2}/S_{P4}	$(1+\theta-\alpha_1)d \le \alpha_1$	$[\alpha_1-\beta, 1]$
	$\beta d \le \alpha_1$	$[-1+\alpha_1+\beta, \alpha_1-\beta)$
	$(\alpha_1-\theta)d \le \alpha_1$	$[-1, -1+\alpha_1+\beta)$
S_{P7}/S_{P5}	$2(\alpha_2-\theta)d \le \alpha_1+\alpha_2$	$[\alpha_2-\beta, 1]$
	$2\beta d \le \alpha_1+\alpha_2$	$[-1+\alpha_2+\beta, \alpha_2-\beta)$
	$2(1+\theta-\alpha_2)d \le \alpha_1+\alpha_2$	$[-1, -1+\alpha_2+\beta)$
S_{P1}/S_{P3}	$2(1-\theta-\alpha_2)d \le \alpha_1+\alpha_2$	$[1-\alpha_2-\beta, 1]$
	$2\beta d \le \alpha_1+\alpha_2$	$[\beta-\alpha_2, 1-\alpha_2-\beta)$
	$2(\alpha_2+\theta)d \le \alpha_1+\alpha_2$	$[-1, \beta-\alpha_2)$
S_{P8}/S_{P6}	$(1-\theta-\alpha_1)d \le \alpha_1$	$[1-\alpha_1-\beta, 1]$
	$\beta d \le \alpha_1$	$[\beta-\alpha_1, 1-\alpha_1-\beta)$
	$(\alpha_1+\theta)d \le \alpha_1$	$[-1, \beta-\alpha_1)$
S_{S1}/S_{S2}	$\beta d \ge 1-\theta-\beta$	$[1-\alpha_1-\beta, 1]$
	$2\beta d \ge 1-\theta+\alpha_1-\beta$	$[1-\alpha_2-\beta, 1-\alpha_1-\beta)$
	$2\beta d \ge \alpha_1+\alpha_2$	$[\alpha_2-\beta, 1-\alpha_2-\beta)$
	$2\beta d \ge \theta+\alpha_1+\beta$	$[\alpha_1-\beta, \alpha_2-\beta)$
	$\beta d \ge \theta+\beta$	$[-1, \alpha_1-\beta)$
S_{S4}/S_{S3}	$\beta d \ge -\theta+\beta$	$[1-\alpha_1+\beta, 1]$
	$2\beta d \ge -\theta+\alpha_1+\beta$	$[1-\alpha_2+\beta, 1-\alpha_1+\beta)$
	$2\beta d \ge \alpha_1+\alpha_2$	$[\alpha_2+\beta, 1-\alpha_2+\beta)$
	$2\beta d \ge 1+\theta+\alpha_1-\beta$	$[\alpha_1+\beta, \alpha_2+\beta)$
	$\beta d \ge 1+\theta-\beta$	$[-1, \alpha_1+\beta)$

a wide range of θ values. An attempt has been made to plot the black dashed lines in Fig. 6, which seems to ensure ZVS across the largest possible θ range in the simplest manner.

It is evident that the position of the black dashed lines varies in different ZVS range, i.e., the best voltage conversion ratio d changes due to different sets of α_1, α_2, and β. Practically, d is determined by the parameter design and can be considered known. Thus, we need to select appropriate phase-shift values according to d. The outer phase-shift value θ is typically used to meet the transmission power requirements, while the inner phase-shift values α_1, α_2, and β are three degrees of freedom to be specified, which can be utilized to achieve optimization goals such as ZVS. When three inner phase-shift values are the same as that of Fig. 6(d), full ZVS can theoretically be realized across the entire θ range at $d = 1$. In comparison, when three inner phase-shift values are the same as that of Fig. 6(c), the θ range for full ZVS becomes much smaller at $d = 1$, but it can achieve full ZVS at $d = 5/3$. To optimize the selection of inner phase-shift values to achieve the widest ZVS range at a fixed d, we can derive a formula that defines the black dashed line (representing the relationship between θ and d). This formula reveals that for every possible combination of inner phase-shift values, there is an associated optimal d. By applying this formula, the inner phase-shift values can be systematically determined to maximize the ZVS operating region. Specifically, this ensures the largest possible range of θ within the gray ZVS area, which corresponds vertically to the chosen d value.

According to previous analysis, when $\alpha_1 \le \alpha_2$, the outer ZVS boundary is delineated by the purple, green lines, dark blue, and blue lines. To derive the analytical expression of the chosen trajectory, we need to first obtain the coordinates of the intersection points of the purple and green lines, as well as the dark blue and blue lines. For example, to get the coordinates of the intersection point of the purple and green lines, the boundary equations of the two lines are simultaneously solved

$$\begin{cases} 2d\sum_{k=1,3,5\cdots}^{+\infty} \frac{\sin(k\beta\pi)\sin[k(\alpha_1+\theta)\pi]}{k^2} \\ = \sum_{k=1,3,5\cdots}^{+\infty} \frac{[\sin(k\alpha_1\pi)+\sin(k\alpha_2\pi)]\sin(k\alpha_1\pi)}{k^2} \\ 2d\sum_{k=1,3,5\cdots}^{+\infty} \frac{\sin(k\beta\pi)\sin(k\beta\pi)}{k^2} \\ = \sum_{k=1,3,5\cdots}^{+\infty} \frac{[\sin(k\alpha_1\pi)+\sin(k\alpha_2\pi)]\sin[k(\theta+\beta)\pi]}{k^2}. \end{cases} \tag{15}$$

By making each harmonic component satisfy the equation and eliminating α_2, the horizontal coordinate can be solved as

$$\theta = 1 - \alpha_1 - \beta. \tag{16}$$

Subsequently, the vertical coordinate of the intersection point can be obtained as

$$d = \frac{\sum_{k=1,3,5\cdots}^{+\infty} \frac{1}{k^2}\left[\sin(k\pi\alpha_1) + \sin(k\pi\alpha_2)\right]\sin(k\pi\alpha_1)}{2\sum_{k=1,3,5\cdots}^{+\infty} \frac{1}{k^2}\sin^2(k\pi\beta)}. \tag{17}$$

Based on the mathematical derivation process presented in Appendix B, (B3) can be used to simplify (17) as

$$d = \frac{\alpha_1}{\beta}\left(0 \le \alpha_2 - \alpha_1 \le 1, 0 \le \alpha_2 + \alpha_1 \le 1\right). \tag{18}$$

The coordinates of the intersection point of the purple and green line are $(1-\alpha_1-\beta, \alpha_1/\beta)$. Similarly, the coordinates of the intersection point of the dark blue and blue line are $(-1+\alpha_1+\beta, \alpha_1/\beta)$. Therefore, the ZVS optimization method for inner phase-shift values is given by (18). Table I also validates this formula, as it coincides with one part of the primary-side boundaries.

With the simple ZVS optimization method, we can decide the relationship of α_1 and β after d is given. Since (18) utilize only one degree of freedom, the remaining ones can be used for other optimization goals, such as minimum current stress.

In addition, the coordinates of the intersection points of the yellow and green lines, as well as the orange and blue lines are $(1-\alpha_2-\beta, (\alpha_1+\alpha_2)/(2\beta))$, and $(-1+\alpha_2+\beta, (\alpha_1+\alpha_2)/(2\beta))$. In fact, α_1 and α_2 have similar impacts on the ZVS range. When $\alpha_2 \le \alpha_1$, the orange line lies outside the dark blue line, and the yellow line locates outside the purple line, i.e., the final ZVS boundaries are determined by the orange, yellow, blue, and green lines. The intersection coordinates of the four intersection points will be $(1-\alpha_2-\beta, \alpha_2/\beta)$, $(-1+\alpha_2+\beta, \alpha_2/\beta)$, $(1-\alpha_1-\beta, (\alpha_1+\alpha_2)/(2\beta))$, and $(-1+\alpha_1+\beta, (\alpha_1+\alpha_2)/(2\beta))$.

C. Expansion of the ZVS Optimization Strategy to ML/NL DAB

Based on the previous derivation, (18) corresponding to the dashed black line is similar to that of a two-level system [13], thus the ZVS constraints proposed before may hold the potential for extension to *M*L/*N*L DAB converters (both M and N are odd numbers apart from equaling to two for a two-level system). With inner phase-shift values α_h ($h = 12, \ldots, M-1$) of primary side and β_l ($l = 12, \ldots, N-1$) of secondary side, the ac-side voltage waveform on the primary side can be composed as a superposition of $(M+1)$ square waves, while the ac-side voltage waveform on the secondary side can be formed as a superposition of $(N+1)$ square waves, as shown in Fig. 7. Each square wave

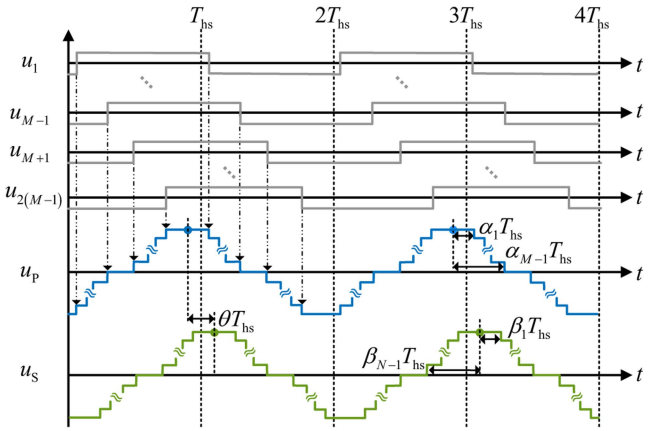

Fig. 7. Schematic diagram of AC-side voltage decomposition for the *M*L/*N*L DAB converter.

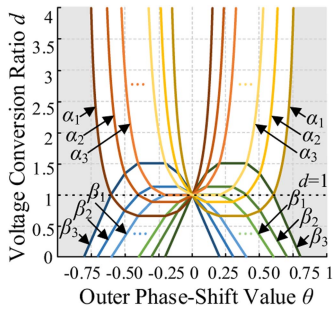

Fig. 8. Ideal ZVS range of the *M*L/*N*L DAB converter.

is of 50% duty ratio. Thus, the ac-side voltages u'_{P} and u'_{S} can be formulated as

$$u'_{\mathrm{P}} = \sum_{i=1}^{2(M-1)} u_{1i},\ u'_{\mathrm{S}} = \sum_{j=1}^{2(N-1)} u_{2j} \tag{19}$$

where

$$u_{1i} = \begin{cases} \frac{2U_1}{(M-1)\pi} \sum_{k=y1,3,5\cdots}^{+\infty} \frac{1}{k} \sin\left[k(\omega t + \frac{\theta}{2}\pi - \alpha_i \pi)\right], i \le M-1 \\ -\frac{2U_1}{(M-1)\pi} \sum_{k=1,3,5\cdots}^{+\infty} \frac{1}{k} \sin\left[k(\omega t + \frac{\theta}{2}\pi + \alpha_{i/2}\pi)\right], i \ge M+1 \end{cases}$$

$$u_{2j} = \begin{cases} \frac{2U_2}{(N-1)\pi} \sum_{k=1,3,5\cdots}^{+\infty} \frac{1}{k} \sin\left[k(\omega t - \frac{\theta}{2}\pi - \beta_i \pi)\right], i \le N-1 \\ \frac{2U_2}{(N-1)\pi} \sum_{k=1,3,5\cdots}^{+\infty} \frac{1}{k} \sin\left[k(\omega t - \frac{\theta}{2}\pi + \beta_{i/2}\pi)\right], i \ge N+1. \end{cases}$$

Similar to the three-level DAB converter, the ac-side currents can be derived by applying the Fourier series expansion and the phasor theory. Considering the ideal ac coupling network, the specific ZVS boundaries for α_h ($h = 12,\ldots,M-1$) and β_l ($l = 12,\ldots,N-1$) can be given as (20)–(23) shown at the bottom of this page, after simplification.

Without loss of generality, assuming $\alpha_1 \le \alpha_2 \le \ldots \le \alpha_{M-1}$, $\beta_1 \le \beta_2 \le \ldots \le \beta_{N-1}$, ZVS range can be visualized in Fig. 8, where the lines in orange, yellow, blue, and green represent the ZVS boundaries shown in (20), (21), (22), and (23), respectively. It can be noted that smaller α_h will lead to a shift of the boundaries defined by (20) and (21) further towards the bottom-left and bottom-right corners, respectively. Also, smaller β_l will cause the boundaries defined by (22) and (23) to shift towards upper right and upper left, respectively. Therefore, the smallest α_h and β_l will generate the smallest ZVS range and determine the final ZVS range. The formula of ZVS optimization for *M*L/*N*L DAB converter is

$$d = \frac{\alpha_1}{\beta_1}. \tag{24}$$

IV. Impacts of Nonideal Factors on ZVS Range of Three-Level DAB Converters

A. Dead Time

Theoretically, a ZVS transition occurs when (7) is satisfied, achieving an instantaneous voltage transition between $0.5U_1$ and 0 or $-0.5U_1$ and 0, as the corresponding switching device is turned OFF. However, in practical applications, the ac-side currents must be sufficiently negative to avoid crossing zero during dead time, as this would result in a partial hard-switching

$$\frac{d}{N-1} \sum_{k=1,3,5\cdots}^{+\infty} \frac{1}{k^2} \left[\sum_{g=1}^{N-1} \sin(k\beta_g \pi)\right] \sin\left[k\left(\alpha_h - \theta\right)\pi\right] < \frac{1}{M-1} \sum_{k=1,3,5\cdots}^{+\infty} \frac{1}{k^2} \left[\sum_{f=1}^{M-1} \sin(k\alpha_f \pi)\right] \sin\left(k\alpha_h \pi\right) \tag{20}$$

$$\frac{d}{N-1} \sum_{k=1,3,5\cdots}^{+\infty} \frac{1}{k^2} \left[\sum_{g=1}^{N-1} \sin(k\beta_g \pi)\right] \sin\left[k\left(\alpha_h + \theta\right)\pi\right] < \frac{1}{M-1} \sum_{k=1,3,5\cdots}^{+\infty} \frac{1}{k^2} \left[\sum_{f=1}^{M-1} \sin(k\alpha_f \pi)\right] \sin\left(k\alpha_h \pi\right) \tag{21}$$

$$\frac{d}{N-1} \sum_{k=1,3,5\cdots}^{+\infty} \frac{1}{k^2} \left[\sum_{g=1}^{N-1} \sin(k\beta_g \pi)\right] \sin\left(k\beta_l \pi\right) > \frac{1}{M-1} \sum_{k=1,3,5\cdots}^{+\infty} \frac{1}{k^2} \left[\sum_{f=1}^{M-1} \sin(k\alpha_f \pi)\right] \sin\left[k\left(\beta_l + \theta\right)\pi\right] \tag{22}$$

$$\frac{d}{N-1} \sum_{k=1,3,5\cdots}^{+\infty} \frac{1}{k^2} \left[\sum_{g=1}^{N-1} \sin(k\beta_g \pi)\right] \sin\left(k\beta_l \pi\right) > \frac{1}{M-1} \sum_{k=1,3,5\cdots}^{+\infty} \frac{1}{k^2} \left[\sum_{f=1}^{M-1} \sin(k\alpha_f \pi)\right] \sin\left[k\left(\beta_l - \theta\right)\pi\right] \tag{23}$$

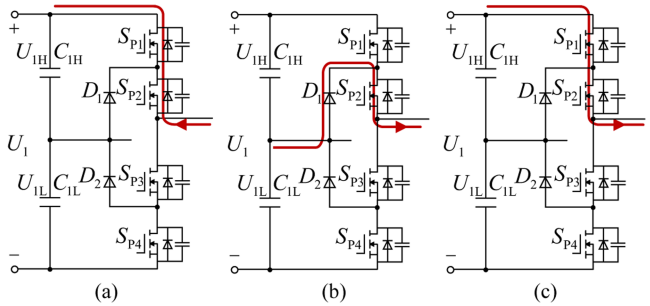

Fig. 9. Partial hard switching event due to dead time. (a) S_{P2} is activated and S_{P3} turns OFF with $i_P<0$ at the beginning of dead time. (b) Only S_{P2} is activated with $i_P>0$ during dead time. (c) S_{P1} turns ON with $i_P>0$ after dead time.

event. One possible hard-switching event due to dead time are depicted in Fig. 9. Instead of ideal voltage transition $0\rightarrow 0.5U_1$, a shift in i_P from negative to positive causes unexpected voltage transition $0\rightarrow 0.5U_1\rightarrow 0\rightarrow 0.5U_1$ during the dead time between the turn-OFF of S_{P3} and the turn-ON of S_{P1}. Therefore, we must ensure that both i_P and i_S remain their polarity during the dead time.

Since the voltage across the leakage inductance remains unchanged, negative currents at the beginning and the end of the dead time are sufficient to meet the demand. The impact of dead time can be readily incorporated using harmonic analysis

$$\begin{cases} \max i_P(t_{P2}+\lambda\delta_{DT\_P}T_s)\le 0, \max i_P(t_{P7}+\lambda\delta_{DT\_P}T_s)\le 0 \\ \max i_P(t_{P1}+\lambda\delta_{DT\_P}T_s)\le 0, \max i_P(t_{P8}+\lambda\delta_{DT\_P}T_s)\le 0 \\ \max i_S(t_{S1}+\lambda\delta_{DT\_S}T_s)\le 0, \max i_S(t_{S4}+\lambda\delta_{DT\_S}T_s)\le 0 \end{cases} \tag{25}$$

where λ is either 0, which indicates the beginning of the dead time, or 1, which denotes the end of the dead time. δ_{DT_P} and δ_{DT_S} represent the ratios of the dead time on the primary and secondary side, respectively, to the switching period. The modified ZVS range considering dead time is shown in Fig. 10.

The solid lines correspond to the ZVS boundaries when $\lambda=1$ and the dashed lines denote the boundaries when $\lambda=0$. To enhance the visibility of the impact of nonideal factors, we set δ_{DT_P} and δ_{DT_S} to be 0.1. The dead time results in a rightward shift of the primary-side boundaries and a leftward shift of secondary-side boundaries. The resultant ZVS range, which is the union of the ZVS ranges when $\lambda=0$ and $\lambda=1$, as denoted by the grey area in Fig. 10. After taking dead time into consideration, the ZVS range changes, but (18), represented by the dashed black line, still maintains a broad ZVS range.

B. Switching Devices' Capacitance

If the drain-source capacitance of the switching devices is substantial or snubber capacitors are added, ac-side currents should be sufficiently negative to ensure full charging or discharging of parasitic capacitance of switching devices turned OFF or turned on. Simple adaptation can be applied to give the ZVS condition considering devices' capacitance

$$\begin{cases} \max i_P(t_{Pi}+\lambda\delta_{DT\_P}T_s)\le -\Delta i_P (i=2,7,1,8) \\ \max i_S(t_{Sj}+\lambda\delta_{DT\_S}T_s)\le -\Delta i_S (j=1,4) \end{cases} \tag{26}$$

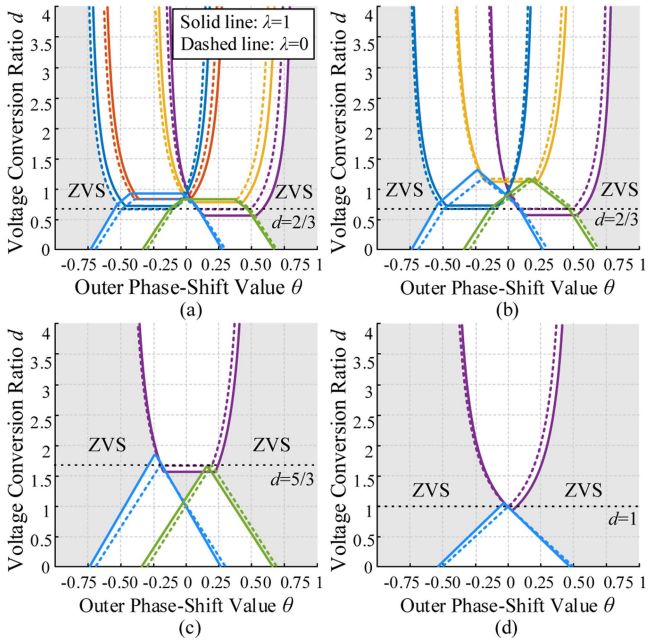

Fig. 10. ZVS range when $\delta_{DT\_P}=\delta_{DT\_S}=0.1$. (a) $\alpha_1=0.2$, $\alpha_2=0.3$, $\beta=0.3$. (b) $\alpha_1=0.2$, $\alpha_2=0.5$, $\beta=0.3$. (c) $\alpha_1=0.5$, $\alpha_2=0.5$, $\beta=0.3$. (d) $\alpha_1=0.5$, $\alpha_2=0.5$, $\beta=0.5$.

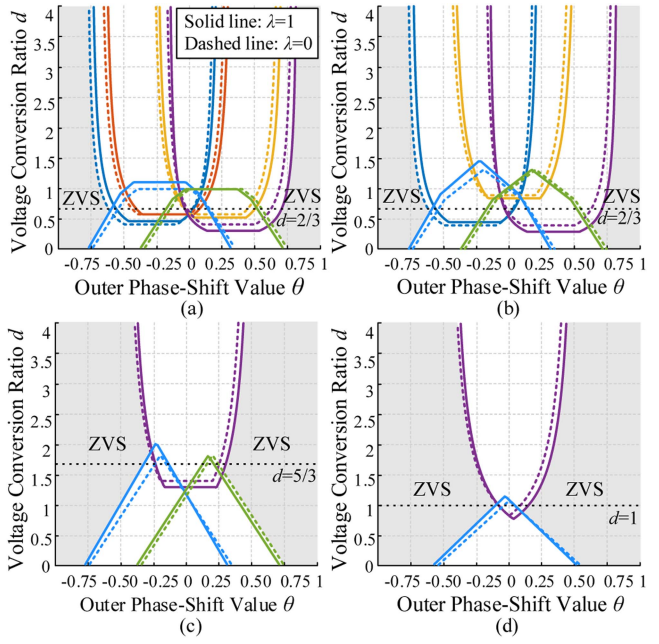

Fig. 11. ZVS range considering dead time and switching devices' capacitance when $\Delta i_P=\Delta i_S=1$ A. (a) $\alpha_1=0.2$, $\alpha_2=0.3$, $\beta=0.3$. (b) $\alpha_1=0.2$, $\alpha_2=0.5$, $\beta=0.3$. (c) $\alpha_1=0.5$, $\alpha_2=0.5$, $\beta=0.3$. (d) $\alpha_1=0.5$, $\alpha_2=0.5$, $\beta=0.5$.

where Δi_P and Δi_S are the minimal ac-side currents to realize full charging and discharging of output parasitic capacitance as one full bridge is switched [15]. Fig. 11 illustrates the ZVS range considering both the dead time and the capacitance of the switching devices. The solid lines show the boundaries when $\lambda=1$ and the dashed lines represent the boundaries when $\lambda=0$.

TABLE II
PARAMETERS OF THE THREE-LEVEL DAB PROTOTYPE

Items	Description	Specifications
U_1	Primary-side dc-link rated voltage	400 V
U_2	Secondary-side dc-link rated voltage	150 V
f_s	Switching frequency	20 kHz
L_k	Leakage inductance	840 μH
n	Turns ratio	2
S_{P1}–S_{P8}	Primary-side switching devices	F3L75R07W2E3_B11
S_{S1}–S_{S4}	Secondary-side switching devices	IMZ120R030M1H
C_{1H}, C_{1L}	Primary-side dc-link capacitance	890 μF
C_2	Secondary-side dc-link capacitance	2.35 mF
C_{BP}, C_{BS}	Dc blocking capacitance	90 μF

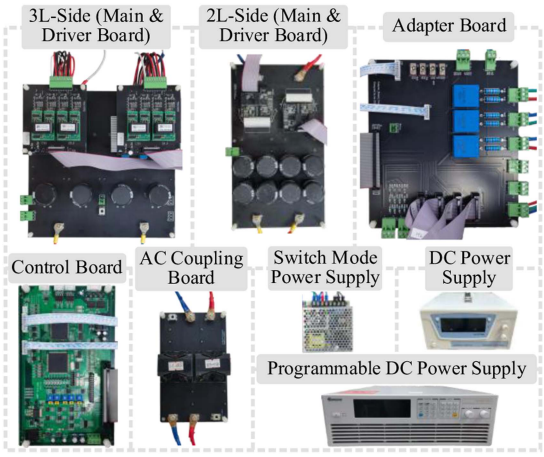

Fig. 12. Experimental platform of the three-level DAB converter.

Compared with Fig. 10, the capacitance of the switching devices causes a downward shift of the ZVS boundary of the primary-side devices and an upward shift for the secondary side devices. It is noteworthy that (18) still implements a large ZVS range even though the ZVS range moves due to the capacitance of the switching devices and dead time. This indicates that (18) can realize full ZVS across widest possible θ range in a simple manner for practical applications.

V. SIMULATION AND EXPERIMENTAL VALIDATION

A. Experimental Validation of the Three-level DAB Converter

An experimental platform of three-level DAB converter is constructed, featuring a 400 V rated voltage on the primary side and 200 V on the secondary side. The ac coupling unit comprises an HFT, a high-frequency inductor and two blocking capacitors. The specifications of the prototype are detailed in Table II, and the photograph of the platform is shown in Fig. 12.

Experiments have been performed to validate (18) and the derived ZVS boundaries with nine operation points under three test conditions, as marked in Fig. 13. The ac-side voltages and currents of the three-level DAB converter at the operating points denoted by the asterisks, dots, and diamonds are shown in Figs. 14, 15, and 16, respectively. The parameters are listed in Table III. Ideally, the intersection purple and green lines

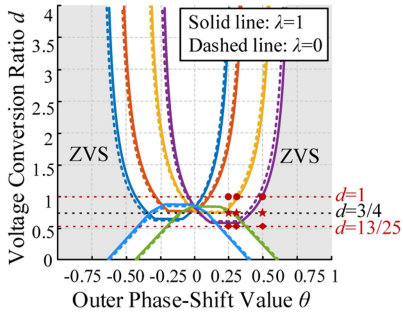

Fig. 13. Practical ZVS range when $\alpha_1 = 0.3$, $\alpha_2 = 0.4$, $\beta = 0.4$.

TABLE III
SPECIFIC EXPERIMENTAL CONDITIONS

Conditions	U_1/U_2	Phase-shift values	Whether (18) is satisfied
1	400V/150V	α_1=0.3, α_2=0.4, β=0.4, θ=0.25, 0.3, 0.5	$d = \alpha_1/\beta = 3/4$
2	400V/200V		$d > \alpha_1/\beta = 3/4$
3	400V/50V		$d < \alpha_1/\beta = 3/4$

corresponding to critical ZVS has the horizontal coordinate of 0.3. By considering complex ac coupling network in Fig. 5 and nonideal factors mentioned before, the practical ZVS range shift. Neutral-point voltage balancing strategy in [16] was adopted to guarantee the reliable operation.

The switching instants of the devices are marked by red dashed lines, with corresponding ac-side currents indicated by red dots. The gray dashed line signifies zero current. Red dots above this line denote positive currents, while those below indicate negative currents. As shown in Fig. 14(c), when (18) is satisfied, full ZVS is realized with negative currents at $\theta = 0.5$. For $d > \alpha_1/\beta$, S_{P8} (S_{P6}) approaches its ZVS boundary, as illustrated in Fig. 15(c). Fig. 16(c) shows a similar case where S_{S1} fails to achieve ZVS when $d < \alpha_1/\beta$. It is obvious that the range of θ across, which all switching devices can achieve ZVS at $d = 3/4$ is broader than that at $d = 1$ and at $d = 1/4$. In practical applications, (18) may not guarantee the widest ZVS range, however, it can attain a widest possible ZVS range through a simple formula on phase-shift values. Furthermore, (18) can be combined with other optimization objectives to achieve multiobjective optimization.

The derived ZVS boundaries can be validated by the nine operating points. For the operating points denoted by asterisks in Fig. 13, when $\theta = 0.25$, they theoretically reside beyond the ZVS regions of S_{P8} (S_{P6}) and S_{S1}(S_{S2}), specifically below the green line and above the purple line. The corresponding ac-side currents of these switching devices are indeed greater than zero in Fig. 14(a). At $\theta = 0.3$, S_{S1} (S_{S2}) achieves critical ZVS, which is consistent with Fig. 14(b), where the secondary-side current is zero. At $\theta = 0.5$, the operating point is situated within the gray region, enabling full ZVS with negative currents, as shown in Fig. 14(c). For operating points marked by dots, as θ increases, S_{P1}(S_{P3}) moves closer to its ZVS boundary (see the yellow line in Fig. 13) and achieves ZVS at $\theta = 0.3$. S_{P8} (S_{P6}) realizes hard switching because the current flowing through it remains positive albeit approaching zero in Fig. 15. Similarly, for

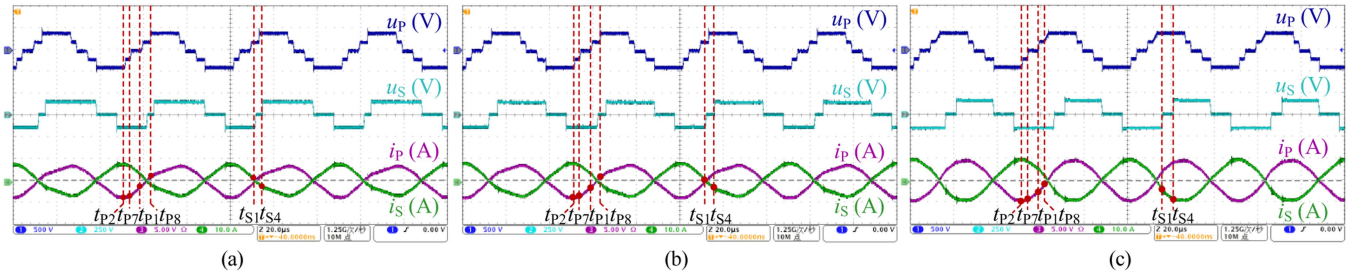

Fig. 14. Experimental results of test condition 1. (a) $\theta = 0.25$. (b) $\theta = 0.3$. (c) $\theta = 0.5$.

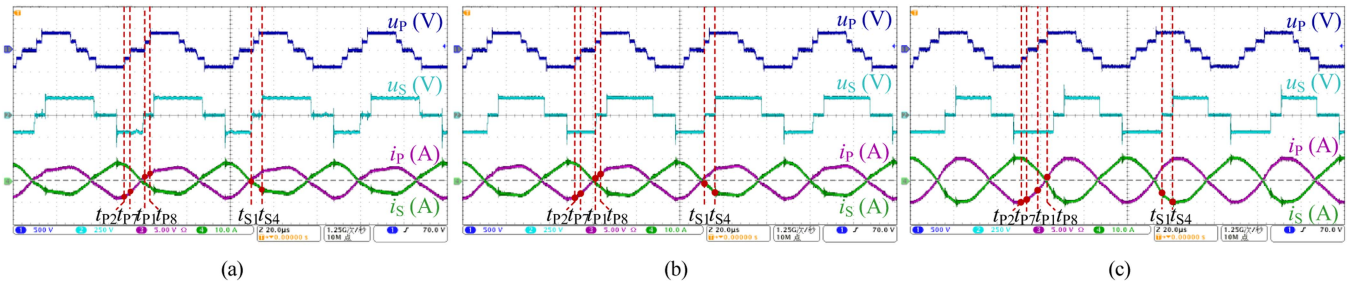

Fig. 15. Experimental results of test condition 2. (a) $\theta = 0.25$. (b) $\theta = 0.3$. (c) $\theta = 0.5$.

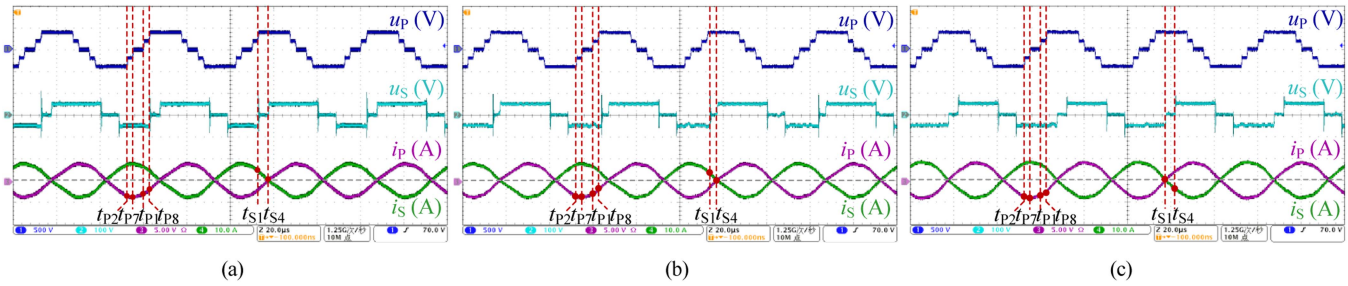

Fig. 16. Experimental results of test condition 3. (a) $\theta = 0.25$. (b) $\theta = 0.3$. (c) $\theta = 0.5$.

operating points marked by diamonds, S_{S4} (S_{S3}) moves closer to its ZVS boundary (see the blue line in Fig. 13) and achieves critical ZVS at $\theta = 0.3$. S_{S1}(S_{S2}) achieves critical ZVS at $\theta = 0.5$, as shown in Fig. 16.

B. Simulation Verification of the Universal ZVS Constraint Conditions for Multilevel DAB

As previously stated, (18) can be extended to (24) for ZVS implementation of *ML*/*NL* DAB converters. To substantiate the proposed universal ZVS constraint (24), a simulation model of a multilevel NPC-DAB converter is built. This model comprises a five-level primary side and a three-level secondary side, with $U_1 = 400$ V, $U_2 = 150$ V, $n = 2$, $\alpha_1 = 0.3$, $\alpha_2 = 0.35$, $\alpha_3 = 0.4$, $\alpha_4 = 0.45$, $\beta_1 = 0.4$, $\beta_2 = 0.45$. The primary-side switching devices are designated as S'_{P1}–S'_{P16}, and the secondary-side ones are denoted by S'_{S1}–S'_{S8}. The ideal ZVS range is illustrated in Fig. 17 and the simulation verification is shown in Fig. 18.

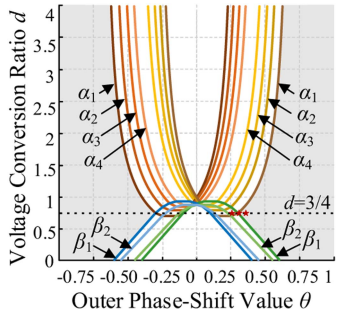

Fig. 17. ZVS range when $U_1 = 400$ V, $U_2 = 150$ V, $n = 2$, $\alpha_1 = 0.3$, $\alpha_2 = 0.35$, $\alpha_3 = 0.4$, $\alpha_4 = 0.45$, $\beta_1 = 0.4$, $\beta_2 = 0.45$.

Three operating points satisfying (24) are selected to validate the ZVS constraint and the derived boundaries for the *ML*/*NL* DAB converter. Based on previous analysis, the coordinates of the intersection of the outermost ZVS boundaries are (± 0.3, 0.75). As illustrated in Fig. 18(b), S_{P16} (S_{P12}) and S_{S2} (S_{S4})

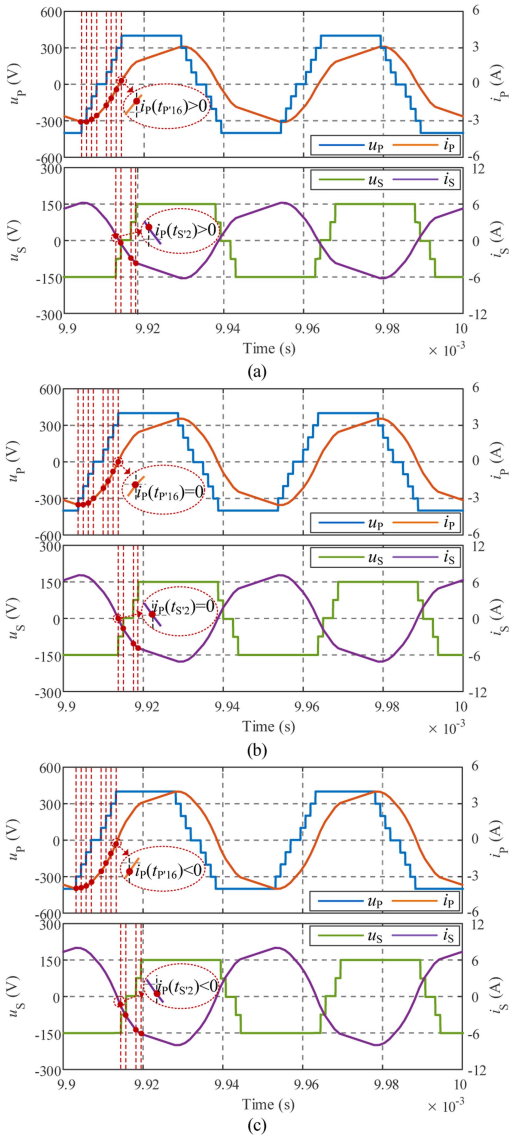

Fig. 18. Simulation results of the 5L/3L DAB converter. (a) $\theta = 0.25$. (b) $\theta = 0.3$. (c) $\theta = 0.35$.

achieve critical ZVS with zero ac-side currents, while all other switches achieve ZVS. When $\theta = 0.25$, the operating points locates above the darkest yellow line and below the darkest green line, so S_{P16} (S_{P12}) and S_{S2} (S_{S4}) fail to achieve ZVS. At $\theta = 0.35$, all switches are able to realize ZVS because the operating point moves into the gray area, thereby validating the universal ZVS constraints.

VI. Conclusion

This study introduces a generalized ZVS optimization strategy on the phase-shift values for three-level DAB converters, and extends it to *M*L/*N*L DAB converters. The proposed strategy enables straightforward implementation of ZVS across a widest possible θ range in practice, thereby improving efficiency of high-frequency operations. Besides, the universal piecewise ZVS boundaries are presented. Both experimental and simulation results validate the derived ZVS ranges and the proposed ZVS optimization strategy under different operating conditions. This research sets the stage for future investigations into multiobjective optimization for multilevel DAB converters, contributing to the advancement of high-performance power conversion systems.

Appendix A
Admittance of Complex HFT Equivalent Circuit

$$\begin{cases} Y^k_{\mathrm{P,P}}\angle\gamma^k_{\mathrm{P,P}} = k\omega C_{\mathrm{BP}}\begin{bmatrix} jk^2\omega^2 C_{\mathrm{BS}}\left(L_{\mathrm{m}}+L'_{\sigma,\mathrm{S}}\right)+ \\ k\omega C_{\mathrm{BS}}\left(R'_{\sigma,\mathrm{S}}+R_{\mathrm{m}}\right)-j \end{bmatrix}\Big/ Z_{\mathrm{eq1}} \\ Y^k_{\mathrm{P,S}}\angle\gamma^k_{\mathrm{P,S}} = -k^2\omega^2 nC_{\mathrm{BP}}C_{\mathrm{BS}}\left(jk\omega L_{\mathrm{m}}+R_{\mathrm{m}}\right)/Z_{\mathrm{eq1}} \\ Y^k_{\mathrm{S,P}}\angle\gamma^k_{\mathrm{S,P}} = -k^2\omega^2 nC_{\mathrm{BP}}C_{\mathrm{BS}}\left(jk\omega L_{\mathrm{m}}+R_{\mathrm{m}}\right)/Z_{\mathrm{eq2}} \\ Y^k_{\mathrm{S,S}}\angle\gamma^k_{\mathrm{S,S}} = k\omega n^2 C_{\mathrm{BS}}\begin{bmatrix} jk^2\omega^2 C_{\mathrm{BP}}\left(L_{\mathrm{m}}+L_{\sigma,\mathrm{P}}\right)+ \\ k\omega C_{\mathrm{BP}}\left(R_{\sigma,\mathrm{P}}+R_{\mathrm{m}}\right)-j \end{bmatrix}\Big/ Z_{\mathrm{eq2}} \end{cases} \tag{A1}$$

where

$$\begin{aligned} Z_{\mathrm{eq1}} &= -k^4\omega^4 C_{\mathrm{BP}}C_{\mathrm{BS}}\left(L_\sigma L_{\mathrm{m}}+L_{\sigma,\mathrm{P}}L'_{\sigma,\mathrm{S}}\right) \\ &\quad + jC_{\mathrm{BP}}C_{\mathrm{BS}}k^3\omega^3\left(R_\sigma L_{\mathrm{m}}+L_\sigma R_{\mathrm{m}}+R'_{\sigma,\mathrm{S}}L_{\sigma,\mathrm{P}}+L'_{\sigma,\mathrm{S}}R_{\sigma,\mathrm{P}}\right) \\ &\quad + k^2\omega^2\left\{C_{\mathrm{BS}}\left[C_{\mathrm{BP}}\left(R_\sigma R_{\mathrm{m}}+R_{\sigma,\mathrm{P}}R'_{\sigma,\mathrm{S}}\right)+L_{\mathrm{m}}+L'_{\sigma,\mathrm{S}}\right]\right. \\ &\quad \left.+C_{\mathrm{BP}}\left(L_{\mathrm{m}}+L_{\sigma,\mathrm{P}}\right)\right\}-jk\omega\left[C_{\mathrm{BP}}\left(R_{\sigma,\mathrm{P}}+R_{\mathrm{m}}\right)\right. \\ &\quad \left.+C_{\mathrm{BS}}\left(R'_{\sigma,\mathrm{S}}+R_{\mathrm{m}}\right)\right]-1 \\ Z_{\mathrm{eq2}} &= -k^4\omega^4 C_{\mathrm{BP}}C_{\mathrm{BS}}\left(L_\sigma L_{\mathrm{m}}+L_{\sigma,\mathrm{P}}L'_{\sigma,\mathrm{S}}\right) \\ &\quad + jC_{\mathrm{BP}}C_{\mathrm{BS}}k^3\omega^3\left(R_\sigma L_{\mathrm{m}}+L_\sigma R_{\mathrm{m}}+R'_{\sigma,\mathrm{S}}L_{\sigma,\mathrm{P}}+L'_{\sigma,\mathrm{S}}R_{\sigma,\mathrm{P}}\right) \\ &\quad + k^2\omega^2\left\{C_{\mathrm{BP}}\left[\left(R_\sigma R_{\mathrm{m}}+R_{\sigma,\mathrm{P}}R'_{\sigma,\mathrm{S}}\right)C_{\mathrm{BS}}+L_{\mathrm{m}}+L_{\sigma,\mathrm{P}}\right]\right. \\ &\quad \left.+C_{\mathrm{BS}}\left(L_{\mathrm{m}}+L'_{\sigma,\mathrm{S}}\right)\right\} \\ &\quad - jk\omega\left[C_{\mathrm{BP}}\left(R_{\sigma,\mathrm{P}}+R_{\mathrm{m}}\right)+C_{\mathrm{BS}}\left(R'_{\sigma,\mathrm{S}}+R_{\mathrm{m}}\right)\right]-1 \\ R_\sigma &= R_{\sigma,\mathrm{P}}+R'_{\sigma,\mathrm{S}}, L_\sigma = L_{\sigma,\mathrm{P}}+L'_{\sigma,\mathrm{S}}. \end{aligned}$$

Appendix B
Derivation of the Key Formula During Deviation Process of the ZVS Optimization Method

In order to simplify (17), even extension is performed to give

$$F(t) = \begin{cases} -f(t), \pi \le t \le 0 \\ f(t), 0 \le t \le \pi \end{cases}. \tag{B1}$$

By expanding it into Fourier series, we can derive

$$t = \frac{\pi}{2} - \frac{4}{\pi}\sum_{k=1,3,5\cdots}^{+\infty}\frac{1}{k^2}\cos(kt), 0 \le t \le \pi. \tag{B2}$$

After applying the product-to-sum identities, (B3) can be deduced that

$$\sum_{k=1,3,5\cdots}^{+\infty}\frac{\sin(kx)\sin(ky)}{k^2} = \frac{\pi y}{4}\left(0 \le x-y \le \pi, 0 \le x+y \le \pi\right). \tag{B3}$$

REFERENCES

[1] B. Zhao, Q. Song, W. Liu, and Y. Sun, "Overview of dual-active-bridge isolated bidirectional DC–DC converter for high-frequency-link power-conversion system," *IEEE Trans. Power Electron.*, vol. 29, no. 8, pp. 4091–4106, Aug. 2014.

[2] N. Hou and Y. W. Li, "Overview and comparison of modulation and control strategies for a nonresonant single-phase dual-active-bridge DC–DC converter," *IEEE Trans. Power Electron.*, vol. 35, no. 3, pp. 3148–3172, Mar. 2020.

[3] L. Yuan, J. Li, Q. Gu, Z. Zhao, and Y. Shen, "Power losses of Si/SiC semiconductors in medium voltage energy router sub-modules with hybrid topology," in *Proc. 20th Int. Conf. Elect. Machines Syst.*, 2017, pp. 1–6.

[4] J. Xu, L. Xu, X. Wang, Y. Xie, Y. He, and X. Ruan, "A multilevel hybrid dual-active bridge DC-DC converter for energy storage system in higher voltage applications," in *Proc. IEEE 11th Int. Symp. Power Electron. Distrib. Gener. Syst.*, 2020, pp. 476–481.

[5] Q. Gu, L. Yuan, S. Yi, J. Nie, and Z. Zhao, "Active selection of current commutation loop for hybrid three-level dual Active bridge DC-DC converter with TPS control," in *Proc. IEEE 10th Int. Symp. Power Electron. Distrib. Gener. Syst.*, 2019, pp. 155–161.

[6] C. Song, Y. Yang, A. Sangwongwanich, Y. Pan, and F. Blaabjerg, "Modeling and analysis of 2/3-lvel dual-active-bridge DC-DC converters with the five-level control scheme," in *Proc. IEEE Appl. Power Electron. Conf. Expo.*, 2021, pp. 1958–1963.

[7] Z. Liu, X. Huang, F. C. Lee, and Q. Li, "Package parasitic inductance extraction and simulation model development for the high-voltage cascode GaN HEMT," *IEEE Trans. Power Electron.*, vol. 29, no. 4, pp. 1977–1985, Apr. 2014.

[8] S. A. Q. Mohammed and J.-W. Jung, "A state-of-the-art review on soft-switching techniques for DC–DC, DC–AC, AC–DC, and AC–AC power converters," *IEEE Trans. Ind. Inform.*, vol. 17, no. 10, pp. 6569–6582, Oct. 2021, doi: 10.1109/TII.2021.3058218.

[9] L. Jiang et al., "Integrated optimization of dual-active-bridge DC–DC converter with ZVS for battery charging applications," *IEEE J. Emerg. Sel. Topics Power Electron.*, vol. 11, no. 1, pp. 288–300, Feb. 2023.

[10] L. Jin, B. Liu, and S. Duan, "ZVS soft switching operation range analysis of three-level dual-active bridge DC–DC converter under phase shift control strategy," *IEEE Trans. Ind. Appl.*, vol. 55, no. 2, pp. 1963–1972, Mar./Apr. 2019.

[11] J. Riedel, D. G. Holmes, C. Teixeira, and B. P. McGrath, "Harmonic-based determination of soft switching boundaries for 3-level modulated single-phase dual active bridge converters," in *Proc. Inst. Elect. Electron. Engineers*, 2015, pp. 1505–1512.

[12] J. Riedel, D. G. Holmes, and B. P. McGrath, "Identifying ZVS soft switching boundaries for bi-directional dual active bridge DC-DC converters using frequency domain analysis," in *Proc. 9th Int. Conf. Power Electron. ECCE Asia*, 2015, pp. 771–776.

[13] J. Riedel, D. G. Holmes, B. P. McGrath, and C. Teixeira, "ZVS soft switching boundaries for dual active bridge DC–DC converters using frequency domain analysis," *IEEE Trans. Power Electron.*, vol. 32, no. 4, pp. 3166–3179, Apr. 2017.

[14] B. Khanzadeh and T. Thiringer, "Closed-form ZVS boundaries for three-phase M-level-to-N-level DAB converters with different winding configurations," *IEEE Trans. Power Electron.*, vol. 38, no. 7, pp. 8528–8543, Jul. 2023.

[15] A. Rodríguez, A. Vázquez, D. G. Lamar, M. M. Hernando, and J. Sebastián, "Different purpose design strategies and techniques to improve the performance of a dual active bridge with phase-shift control," *IEEE Trans. Power Electron.*, vol. 30, no. 2, pp. 790–804, Feb. 2015.

[16] C. Song, A. Sangwongwanich, Y. Yang, and F. Blaabjerg, "A model-free capacitor voltage balancing method for multilevel DAB converters," *IEEE Trans. Power Electron.*, vol. 38, no. 1, pp. 79–84, Jan. 2023.

Wei Shao was born in Shandong, China, in 2000. She received the B.S. degree in electrical engineering from Beijing Jiaotong University, Beijing, China, in 2022. She is currently working toward the M.S. degree in power electronics with the School of Electrical Engineering, Beijing Jiaotong University, Beijing, China.

Her current research interests include multilevel converters and DC–DC converters.

Chenchen Wang (Senior Member, IEEE) was born in Anhui, China, in 1981. He received the B.S. and Ph.D. degrees in electrical engineering from Tsinghua University, Beijing, China, in 2003 and 2008, respectively.

He is currently a Professor with the School of Electrical Engineering, Beijing Jiaotong University, Beijing, China. His research interests include electric drives and multilevel converters.

Kai Li (Member, IEEE) received the B.S. degree in electrical engineering from Wuhan University, Wuhan, China, in 2011, and the Ph.D. degree from Tsinghua University, Beijing, China, in 2017.

He was a Visiting Scholar with the Center for Power Electronics Systems, Virginia Tech, Blacksburg, VA, USA, from 2013 to 2015. He was a Postdoctoral Fellow with Tsinghua University, from 2017 to 2019. In 2019, he was with the School of Electrical Engineering, Beijing Jiaotong University, Beijing, China, where he is currently an Associated Professor with the School of Electrical Engineering. His current research interests include solid-state transformer, railway electrification system, modular multilevel converters, and electrolytic hydrogen production converters.

Zhibo Zhang (Graduate Student Member, IEEE) was born in Tieling, China, in 1996. He received the B.S. degree in electrical engineering in 2019 from Beijing Jiaotong University, Beijing, China, where he is currently working toward the Ph.D. degree in power electronics with the School of Electrical Engineering.

His current research interests include railway electrification system and PWM converter.

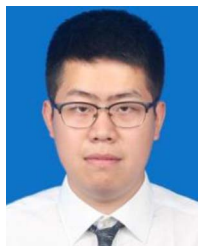

Changyu Gao (Graduate Student Member, IEEE) was born in Jinan, China, in 1997. He received the B.S. degree in electrical engineering from Shandong University of Science and Technology, Qingdao, China, in 2019. He is currently working toward the Ph.D. degree in electrical engineering with Beijing Jiaotong University, Beijing, China.

His current research interests include multiport DC–DC converters and solid-state-transformers.